Gas permeability of Ti6Al4V foams prepared via gelcasting, experiments and modelling

J. Lux, E. Guzi De Moraes, E. Maire, Jérôme Adrien, L. Biasetto

Gas permeability of Ti6Al4V foams prepared via gelcasting, experiments and modelling

Jérôme Lux[a,*], Elisangela Guzi de Moraes[b,1], Eric Maire[c], Jérôme Adrien[c], Lisa Biasetto[d]

[a] Laboratoire des Sciences de l'Ingénieur pour l'Environnement UMR CNRS 7356, Pôle Sciences et Technologie, Avenue Michel Crépeau, 17042 La Rochelle Cedex 1, France
[b] Departimento di Tecnica e Gestione dei Sistemi Industriali, Università di Padova, Stradella San Nicola 3, 36100 Vicenza, Italy
[c] Université de Lyon, INSA de Lyon, MATEIS, CNRS UMR5510, F-69621 Villeurbanne, France
[d] Dipartimento di Ingegneria Industriale, Università di Padova, Via Marzolo 9, 35131 Padova, Italy

ARTICLE INFO

Keywords:
Metallic foams
Permeability
X-ray computed tomography
Computational fluid dynamics
Morphology

ABSTRACT

The use of light components possessing tailored functional properties will represent one of the main issues for the development of new products. Open cells foams, where porosity is engineered in order to grant for lightness, high geometrical surface, interconnectivity and permeability, can be shaped using various techniques and possess regular or irregular structure. In this work, Ti6Al4V foams were produced using the gelcasting route, a technique usually employed for ceramics. Numerical simulations were carried out directly on 3D images of the foam's microstructure obtained by X-ray 3D μCT in order to predict the gas permeability properties of the produced samples. The obtained results were compared to experimental measurements of gas permeability. This approach could be useful for the prediction of Newtonian fluids permeability behavior of non-periodic and complex porous structures.

1. Introduction

Metallic foams offer a set of intriguing functional and structural properties in terms of high specific stiffness, impact and energy absorption. They can be used as filters and heat exchangers (open cells) or as thermal and acoustic insulators (close cells). Depending on their composition, they may find applications in different fields such as building (aluminum foams panels for facades and floors), automotive (sandwiches cores for lightweight vehicles, nickel-based cathode substrates for high efficiency batteries, titanium substrates for fuel cells) aeronautic and military (titanium foams for lightweight and high corrosion resistance components), biomedical (Ti6Al4V alloy foams for bone replacements) [1–3]. The use of metallic foams may represent a double advantage in terms of reduction of the use of raw materials and weight reduction of the final component (porosity is an empty phase). These two aspects make metallic foams a cutting edge material for circular economy European policies. However, wide scale applications are still limited by the high production costs, that make metallic foams often non-competitive in comparison to the polymer-based cheaper solutions.

Authors recently reported on the production of Ti6Al4V open-cell foams by a novel gelcasting route [4]. The effect of processing parameters on foams morphology and composition were studied. Foams with a porosity ranging from 71 to 91 vol% and compression yield strength from 24 MPa up to 79 MPa were produced. The foams exhibited a double pore size distribution with large pores (530–730 μm) and smaller pores (79–124 μm), with large pores deriving from the air bubbles incorporated during the process and small pores deriving from empty spaces around the titanium spherical particles due to uncomplete sintering.

In the present work, optimized process parameters were used to produce Ti6Al4V foams possessing two different range of porosity and pores size. Their morphology was studied by means of X-ray micro-Computed Tomography (3D μCT). Their gas permeability was measured and compared to simulated values. As reported by other authors [5–13], using the Forchheimer equation to calculate the Darcy permeability and the form drag coefficient can lead to significant errors when these coefficients are calculated on experimental data that cover different flow regimes. A complementary approach was used in this paper, which is to perform numerical simulations [14,15] directly on 3D images of the foam's microstructure obtained by X-ray 3D μCT. This is however particularly challenging in this kind of material featuring a non-periodic structure with a wide range of pore size.

* Corresponding author.
E-mail address: jerome.lux@univ-lr.fr (J. Lux).
[1] Present address: Department of Mechanical Engineering – EMC, Federal University of Santa Catarina – UFSC, PO Box 476, University Campus, Florianópolis, Brazil.

Table 1
Overview of main processing parameters and physical properties of Ti6Al4V-700 and Ti6AL4V-1500 samples.

Sample	Mixing Rate [rpm]	T sint [°C]	Density [g/cm^3]	Porosity (Experimental) [vol.%]	Porosity (Image analysis) [vol.%]
Ti6Al4V-700	700	1400	0.79 ± 0.08	81.3 ± 0.5	83.4
Ti6Al4V-1500	1500	1400	1.25 ± 0.01	70.9 ± 0.9	72.2

2. Materials

Foams were prepared as reported in [4]. Briefly, Ti6Al4V powder was added stepwise to the methylcellulose (MC) solutions containing 1 wt% of PEI, a cationic polyelectrolyte, upon continuous stirring with a laboratory mixer for 20 min. Afterwards, the 35 vol% concentrated slurry was aerated with a double shear mixer during 2 min followed by addition of 0.1 vol% of Tergitol™ TMN 10 and subsequently, 5 wt% of ovalbumin (amount calculated based on the metallic powder content) was added, then the suspension was vigorously stirred at different mixing rates (700 rpm or 1500 rpm) during 3 min in order to achieve foaming, and consequently to tailor the pore microstructure and porosity. Afterwards, the foams were poured in a Teflon mold and thermal gelling occurred in a dryer at 80 °C for 2 h. Sintering was conducted in two steps: pre-calcination at 650 °C (2h; 1 °C/min heating rate), to decompose the organic phase; final sintering at 1400 °C (4h, 2 °C/min heating rate) under 99.99% Argon flow and high vacuum. The gas permeability was subsequently measured, and some other samples were cut for the three-dimensional high-resolution X-ray adsorption tomography evaluation. In Table 1 an overview of the processing conditions and sample names is reported.

3. 3D micro-computed tomography (3D µCT)

3.1. Acquisition

X-ray computed tomography was used at two different scales to digitize the morphology of the Ti6Al4V-700 and Ti6Al4V-1500 produced samples. The sample were first cut into parallelepipeds of approximate dimensions (5 × 5 × 20 mm) and scanned at low resolution (lateral voxel size = 7 µm). The tomograph used for this first acquisition is described in [16]. It was operated at 100 kV and 220 µA. This allowed us to analyze the so-called "macro" porosity. 3D visualizations of reconstructed sub-volumes of the 1500 rpm and 700 rpm samples are shown in Fig. 1. This first low scale imaging was not sufficient to capture the smaller pores. The samples were then cut into smaller rods (1 × 1 × 10 mm) and scanned at higher resolution (voxel size = 0.7 µm) using a second tomograph described in [17]. 3D visualizations of reconstructed sub-volume of the high-resolution images of the two samples are shown in Fig. 2.

3.2. Segmentation

Before the image can be analyzed, porous and solid phase must be identified. A simple threshold is applied on the high-resolution images of the two samples as well as the low-resolution image of the Ti6Al4V-700 sample. This gives a sufficiently good segmentation of the two phases. It is however not as simple for the low-resolution image of the Ti6Al4V-1500, because the smallest pores are not well resolved. The grey level of voxels containing both pore and metal is indeed a weighted average of the pore and metal grey levels (partial volume effect). In order to retrieve the majority of the small-scale porosity, the image was then smoothed using a Perona-Malik anisotropic diffusion filter [18] followed by a sharpen filter to enhance the remaining small dark zones that correspond to small-scale porosity. A global threshold was applied and then isolated clusters of white voxels were deleted. The result of this process is shown in Fig. 3. The total porosity measured in the low-resolution image of the Ti6Al4V-1500 sample is 72.2%, which is very close to the experimental data of 70.9% (see Table 1).

3.3. Pore size distribution

A simple way to measure pore size distribution without prior segmentation of individual pores is to perform a granulometry by opening [19,20] on the pore space. An opening is a morphological operation that removes part of the considered set which is strictly smaller that the size of a chosen structuring element (generally a ball or a disk). Using a series of openings of increasing size, the pore size distribution can be deduced from the measures of the number of voxels deleted after each opening.

4. Pressure drop and flow regimes

In past few years, lots of studies have demonstrated the critical importance of determining the different flow regimes prior to evaluating the Darcy permeability and inertia correction [5,7,9–13]. Different flow regimes have been observed in the literature [10,11,21]: Darcy, inertial (weak and strong) and turbulent. It has been shown that the macroscopic equations describing the flow in these different regimes are not the same. Note that the transition between different regimes can also exhibits a different behavior. That's why fitting Forchheimer equation to velocity vs pressure drop curve in order to determine Darcy permeability and inertial coefficient can lead to very different results depending on the range of flow velocity. In a remarkable paper, Lasseux et al. [11] carried out a thorough numerical study of inertial effects in different laminar flow regimes, on ordered and disordered structures. Using the macroscopic flow equation derived from the volume averaging of Navier-Stokes equations, they find that:

- The inertial correction is always characterized by a cubic dependence on the velocity in the weak inertia regime but is generally insignificant except in the case of ordered structures with particular pressure gradient orientations.
- The Forchheimer correction (e.g. a quadratic dependence on the velocity) is a robust approximation in a very large interval of Reynolds numbers, on disordered structure (note that this is not always the case on ordered structures). The correction is not purely quadratic, but of the form $av + bv^2$, which explain why the permeability measured in inertia regime is not the same as the Darcy permeability.

In order to identify flow regimes, some authors [10] use the Forchheimer number defined as:

$$F_o = \frac{\rho v_s (K_D \cdot \beta)}{\mu} \tag{1}$$

where K_D is the Darcy permeability (m^2), β is the inertial coefficient (m^{-1}), μ the viscosity (Pa s), ρ is the fluid density (kg m^{-3}) and v_s is the superficial velocity (m s^{-1})

The problem is that both K_D and β have to be known beforehand.

In the case of porous media with large pore size distribution, it is also possible to define a Reynolds number using $\sqrt{K_D}$ as a characteristic length [11,21]:

$$Re_K = \frac{\rho v_s \sqrt{K_D}}{\mu} \tag{2}$$

which can also be used to identify flow regimes. Some correlations between threshold Re_K and porosity are given in [11], but it is far from certain that these are also valid for other structures.

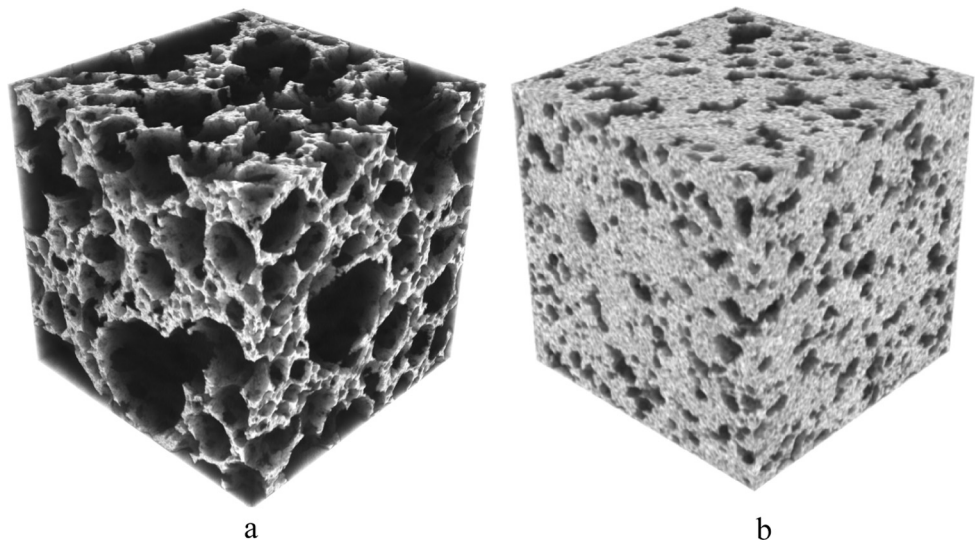

Fig. 1. (a) 3D visualization of the low-resolution image of the Ti6Al4V-700 sample (5.4 × 5.4 × 5.4 mm^3, resolution 14 µm/voxels – after binning of the initial reconstruction) and (b) of Ti6Al4V-1500 sample (2.8 × 2.8 × 2.8 mm^3, resolution 7 µm/voxels – no binning). Solid matrix in light grey.

The other way to identify flow regimes is simply to plot some meaningful data (pressure gradient, reduced pressure gradient $\frac{\Delta P}{Lv_s}$, etc.) vs velocity or, if available, Re_K [5,10,21]. This graphical method can however be error-prone due to dispersion of experimental data, small number of data points, etc.

In the Darcy regime and assuming a one-dimensional pressure gradient, we have the following macroscopic relation:

$$-\frac{\partial P}{\partial x} = \frac{\Delta P}{L} = \frac{\mu}{K_{\mathrm{D}}} v_s \tag{3}$$

where ΔP is the pressure drop and L is the medium thickness along the macroscopic flow direction (m).

In the strong inertia regime, the Forchheimer equation can be written:

$$-\frac{\partial P}{\partial x} = \frac{\Delta P}{L} = \frac{\mu}{K_F} v_s + \rho\beta v_s^2 \tag{4}$$

where K_F is the Forchheimer permeability (m^2), which is different from the Darcy permeability.

As stated previously, the Darcy permeability have to be estimated in Darcy regime using Eq. (3) and K_F and β have to be estimated in the inertia regime using Eq. (4).

(4 can be modified to take into account compressible effects. If we assume that the gas is ideal, it gives, after integration of Eq. (4) between $x = 0$ and $x = L$ [22]:

$$\frac{P_{in}^2 - P_{out}^2}{2P_{out}L} = \frac{\mu}{K_F} v_s + \rho\beta v_s^2 \tag{5}$$

where P_{in} and P_{out} are, respectively, the absolute fluid pressure at the entrance and at the exit of the medium.

Another critical point in the determination of gas permeability of metallic foams is the measurement of the pressure drop ΔP through the sample thickness. In [23] compressibility effects were measured by collecting pressure profiles along the sample thickness (corresponding to the main flow axis). By this route it was confirmed that the macroscopic pressure drop is linear for incompressible fluid (water), whilst it is non-linear in the case of compressible fluids (air). It is clear that pressure measurements at the entrance and exit of fluid flow through

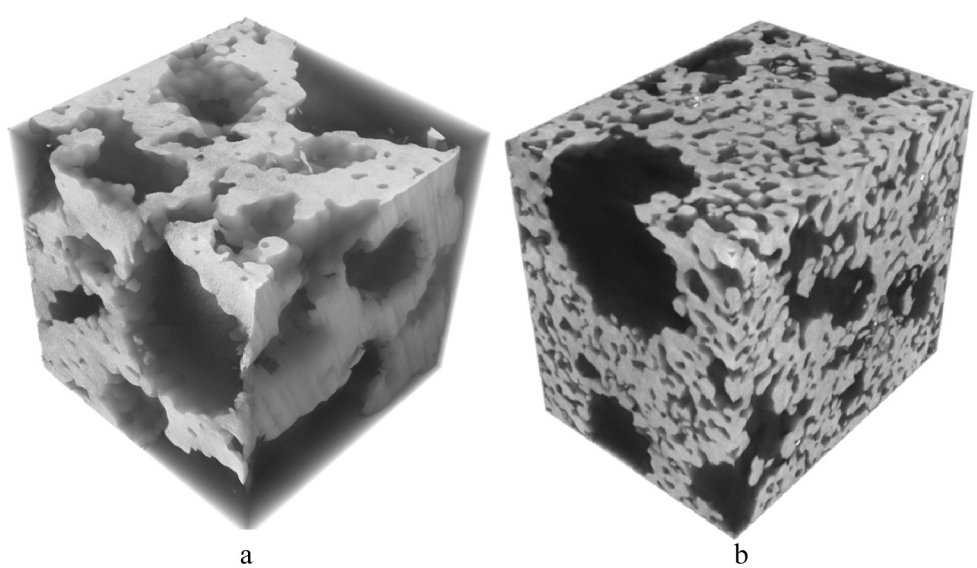

Fig. 2. (a) 3D visualization of the Ti6Al4V-700 sample (0.54 × 0.54 × 0.54 mm^3, resolution 1.4 µm/voxels after binning) and (b) of the high-resolution image of Ti6Al4V-1500 sample (0.47 × 0.58 × 0.63 mm^3, resolution 1.4 µm/voxels after binning). Solid matrix in light grey.

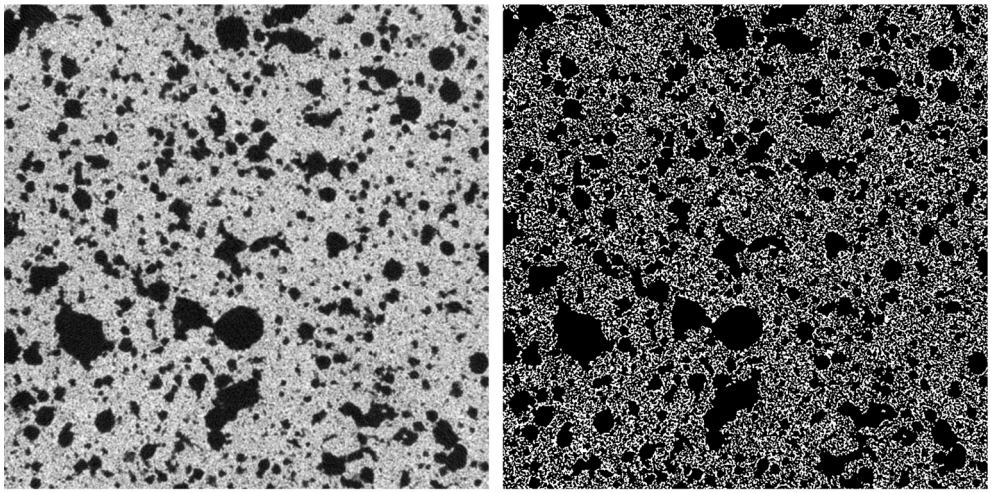

(a) (b)

Fig. 3. Slice (1000 × 1000 pixels) of the low-resolution grey level image (a) and corresponding slice in the binary image (b).

the sample are affected by edges effects and differ from the pressure profiles measured along the sample thickness. However it was also observed that these edge effects can be minimized by reducing the sample thickness and the A_{flow} over A_{sample} ratio [24] without compromising the representativity of the sample.

5. Gas permeability measurements

Permeation experiments were performed on one sample for each composition and were repeated three times, with argon flow at room temperature (20–24 °C) and atmospheric pressure ($P_{atm} = P_{out} \cong 1.025$ bar), that were measured by a thermocouple fixed at the exit of the flow meter and a barometer, respectively. The setup for these measurements was previously described in [25], a scheme of which is reported in Fig. 4.

The disk specimen under analysis was tightly fixed with rubber rings inside the sample holder that provided a useful flow diameter of 14 mm ($A_{flow}/A_{sample} = 0.6$, where A_{flow} is the surface exposed to the fluid flow and A_{sample} is the sample's surface area). As previously observed [24] the sample thickness as well as the A_{flow} over A_{sample} ratio may affect the measurement of permeability constants. Ratios far from 1 give rise to a stagnant space (where the fluid doesn't flow) so to an enlargement of the flow section. Decreasing the sample thickness can reduce this effect. Indeed, our experiments were performed at high A_{flow}/A_{sample} ratios and at low sample thickness (~6 mm). So that we can estimate a reduced flow deformation and a consequent negligible effect on the measurement of the permeability constants.

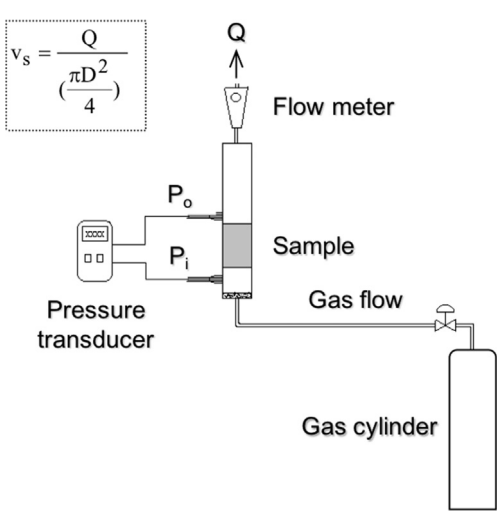

Fig. 4. Schematic drawing of the experimental setup used for the measurement of permeability.

Argon flow from a commercial cylinder (99.9% purity) upward through the disk and was controlled by a needle valve. Pressure drop across the disk (ΔP_{sample}) as well as the pressure drop between the sample exit and the atmosphere (ΔP_{exit}) were measured by a digital manometer (Greisinger electronic GmbH, Germany – model GMH 3161-01 CE, range 0–25 mbar, resolution of 0.01 mbar). The pressure drop parameter used to fit the experimental data was calculated using Eq. (5) with $P_{in} = P_{out} + \Delta P_{sample}$ and $P_{out} = P_{atm} + \Delta P_{exit}$ as previously reported in [25]. The resulting volumetric argon flow rate (Q) across the disk was measured by a rotameter (CT Platon, France model NG GTF2BHS, 1–10 NL/min, resolution of 0.5 NL/min). Argon flow temperature was measured in the exit stream with help of a digital thermometer with a resolution of 0.1 °C. In order to ensure a reliable fitting analysis, at least 15 sets of pressure drop and flow rate were measured in steady-state conditions. The experiment was reproduced three times for each sample.

The collected data were fitted according to the least-square method using a parabolic model of the type $y = ax + bx^2$. Using this procedure and Eq. (5), we have $y = \Delta P/L$, $x = v_s$, $a = \mu/K_F$ and $b = \rho\beta$ so that K_F and β constants can be easily extrapolated from experimental data. Note that we use a one-dimensional Forchheimer equation here, because it was shown in [11] that the Forchheimer correction tensor is diagonal for a disordered isotropic structure when estimated on a Representative Elementary Volume.

6. Numerical methods

3D µCT images show that the Ti6Al4V open-cell metallic foams feature a wide range of pore sizes. The low-resolution image is therefore a compromise between precision and representativity. Furthermore, we'll see later that we cannot be sure that the whole image is sufficiently large to be representative. As a consequence, the main numerical challenge is to be able to perform numerical computations on very large volumes. As it is not tractable to mesh such a large image [14], we use the implicit discretization of the image, i.e. we use voxels as elementary volumes. The main advantage of this approach is that we do not have to remesh the image, we just need to store the binary image and iterate through it to generate the linear systems at each iteration. The main drawback is that it is not easy to refine the mesh near pore/solid interfaces or in small pores.

We developed a homemade c++ code to solve the steady incompressible Navier-Stokes equations directly on binary images:

$$\nabla \cdot \boldsymbol{v} = 0 \tag{6}$$

$$\nabla \cdot (\varrho \boldsymbol{v} \otimes \boldsymbol{v}) = -\nabla p + \mu \Delta \boldsymbol{v} \tag{7}$$

Equations are discretized using a staggered grid and a hybrid differencing scheme. We implemented SIMPLEC, SIMPLER and SIMPLER-R [26] algorithms for pressure-velocity coupling. The SIMPLER-R algorithm was used for the Ti6Al4V-700 sample and for pressure drops over 6×10^3 Pa/m, where SIMPLEC and SIMPLER methods were not able to converge (see the reference book [27] for further details about numerical methods).

To reproduce the experimental setup, a constant pressure is imposed at the inlet and at the outlet, while impervious boundary conditions are imposed on the other faces. No-slip condition is assumed at the solid/air interface.

Simulations are stopped when the relative maximum mass residual as well as the relative momentum components residuals are lower than 10^{-5}.

In a first series of numerical simulations, the Navier-Stokes equations are solved for different pressure gradients ranging from 10^3 to 10^5 Pa/m. In the same way as for experimental measurements, the superficial velocity v_s is measured and the Forchheimer permeability K_F as well as the Forchheimer inertial coefficient β are deduced from a parabolic fit using Eq. (4). In a second series of numerical simulations, we solve the steady Stokes equation (i.e. neglecting the inertial term $\nabla \cdot (\varrho \boldsymbol{v} \otimes \boldsymbol{v})$ in Eq. (7) to compute directly the Darcy permeability K_D. In this case, only one simulation is sufficient, since K_D is a geometrical parameter and therefore does not depend on the pressure drop.

7. Results

7.1. Structural characterization

In Table 1 an overview of the main processing parameters and physical properties after sintering is reported.

Previous 2D morphological analysis [4] have shown that the two samples have different cell size and porosity, as a consequence of the effectiveness of the gelcasting approach employed to stabilize the gas bubbles against the destabilization mechanisms. Thus, some bubbles may shrink and disappear whilst others may coalesce to form larger bubbles [28], due to a thinning process of the particle coating (lamella) surrounding the bubbles, and the consecutive increase of the mechanical shearing [29,30] (up to 1500 rpm); by this route, the cell sizes decreased [31] from 732 to 532 µm, approximately. In addition, the gelation process can also lead to a significant local shrinkage of the wet foam favoring the rupture of the lamella around the bubbles, resulting in the interconnection of cells after drying and sintering. The total porosity of the final porous ceramic is linked to the amount of gas incorporated during the foaming process [28]. SEM images of the two samples show that the microstructure of the Ti6Al4V open-cell metallic foams presents an interconnected network of spherical cells, homogeneously distributed with apparently dense struts (Fig. 5). This is also clearly visible in the 3D µCT images (Figs. 6 and 7). Using µCT, the big pores of the Ti6Al4V-1500 appears to be not always spherical, as opposed to the Ti6Al4V-700 sample, where the pores are also larger. No anisotropy could be noticed in the cellular structure. This was expected, given the process used, where pores are formed by air bubbles gelling and not by gas escape. In the high-resolution image (Fig. 7), we can distinguish a smaller porosity (d < 10 µm) in the cell walls where the Ti6Al4V powders are not in strict contact to each other due to partial sintering. To complete this qualitative analysis, the pore size distribution was measured on the low-resolution image of the two samples (Fig. 8). These results highlight the differences between the two samples. In the Ti6Al4V-700, the small pores in the cell walls represent about 5% of the total porosity, while 50% in the Ti6Al4V-1500 sample (pores size smaller than 50 µm approximately, tallest peak in Fig. 9). For a better precision, Fig. 9 shows the pore size distribution measured in the high-resolution image of the Ti6Al4V-1500 sample, for a pore size range between 2.8 and 50 µm. These results indicate that a more than 50% of the pores in the cell-wall are smaller than 17 µm. In Fig. 8, we can also notice that pores are also bigger in the Ti6Al4V-700 sample: maximum pore size is 2.4 mm vs 0.8 mm in the Ti6Al4V-1500 sample. The average pore size and standard deviation of the Ti6Al4V-700 and Ti6Al4V-1500 samples are 792.5 ± 637.7 µm and 84.9 ± 93 µm respectively (Fig. 7).

7.2. Geometrical representative elementary volume

If the small-scale images are clearly too small to be representative, an important question is to verify if low-resolution images contain a Geometric Representative Elementary Volume (GREV). A simple test is to measure the porosity in series of volumes of increasing sizes centered at different locations in the whole image. Figs. 10 and 11 show the porosity measured in cubes centered at 10 random locations versus the ratio of the cube's volume over the image volume in the two samples. These results show that the porosity is not fully stabilized before reaching the whole volume. However, from volumes of about 30% of the total volume the variation of the measured porosity φ is less than $0.025 \times \varphi_{tot}$, which is a criterion used in previous work [8]. The porosity is however generally not sufficient to conclude about the representativity of a porous medium. In previous numerical studies [8,32], it was found that a computational volume containing about 3 to 4 mean pore diameter per side was sufficient to achieve a good representativity (both geometrically and physically). In our case, there are about 9 mean pores per side in the Ti6Al4V-700 image and 80 mean pores per side in the Ti6Al4V-1500 image. The pore size distributions of the two samples show however an important standard deviation and it could be more relevant to use the maximum pore diameter measured in the pore size distribution. In this case, the number of maximum pore per side is approximately 3 for the Ti6Al4V-700 image and 9 for the Ti6Al4V-1500 image. In view of these results, the image dimensions seem to be large enough to achieve a sufficient geometrical representativity, but only numerical simulations will tell if the volumes are sufficiently large to be representative for the studied phenomenon.

7.3. Gas permeability: experimental results

Typical experimental data of the measure of the pressure gradient defined as $\frac{\Delta P}{L} = \frac{P_{in}^2 - P_{out}^2}{2P_{out}L}$ (see Eq. (5)) as a function of fluid velocity for Ti6Al4V-700 and Ti6Al4V-1500 samples are reported in Fig. 12. In order to identify flow regimes, the reduced pressure gradient $\frac{\Delta P}{Lv_s}$ is plotted against the superficial velocity v_s, as in [5,33] for the Ti6Al4V-1500 sample (Fig. 13) and for the Ti6Al4V-700 sample (Fig. 14). Following the analysis in [5], it seems that the transition between Darcy and inertial regime occurs between 0.12 and 0.24 m s^{-1} for the Ti6Al4V-700 sample, so that a large majority of the data points are in the inertia regime. No clear threshold between weak and strong inertia can be detected here, due to precision of experimental data. For the Ti6Al4V-1500, it seems that the whole data range is in the inertia regime. The Forchheimer regime (i.e. linear part) seems to begin for velocity values greater than 0.6 m s^{-1}. Under that threshold velocity, we observe a transitional regime (possibly mixed with weakly inertial) between Darcy and Forchheimer regime.

In order to compute β and K_F, we fit data points above 0.6 m s^{-1} to Eq. (5) for the Ti6Al4V-1500 sample and above 0.4 m s^{-1} for the Ti6Al4V-700 sample. The Darcy permeability K_D is *estimated* using only the first point (approximately 0.12 m s^{-1} for both samples). Indeed, the reduced pressure gradient is constant vs velocity in the Darcy regime. All these values, as well as the relative difference $\varepsilon = \frac{|K_D - K_F|}{K_D}$, are

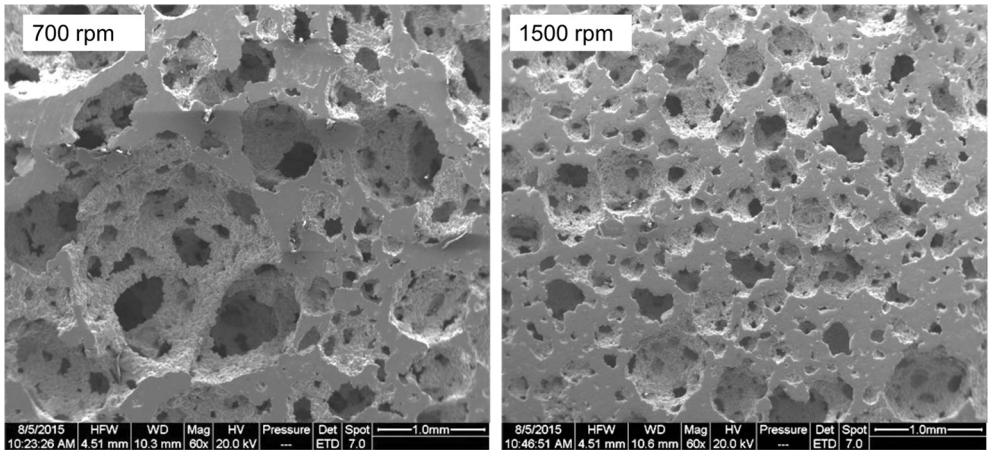

Fig. 5. FEG-SEM pictures of foams processed at 700 rpm (left) and 1500 rpm (right).

reported in Table 2. Standard deviations are given in parenthesis. As expected from previous analysis, K_D and K_F are very close in the case of the Ti6Al4V-1500 sample because the whole data range lies in the inertia regime. It is therefore not possible to estimate K_D with confidence in this case. The difference between K_F and K_D is more important in the case of Ti6Al4V-700 sample, which is expected since the Darcy permeability was estimated using a point at the end of the Darcy regime whereas K_F was estimated only in the inertial regime.

In [11], a correlation between porosity and the Reynolds number at the transition between weak and strong inertia regime (noted Re_{Kc}) was given for disordered structure:

$$Re_{Kc} = 0.69\frac{p^{1.49}}{(1-p)^{0.36}} \tag{8}$$

where p is the porosity.

Values of this crossover Reynolds number for each sample and corresponding velocity computed with Eq. (2) is given in Table 3 for porosity measured experimentally and on tomographic images. The results indicate that the transition velocity determined using the correlation corresponds well with the transition identified graphically. Even if the correlation was obtained for a different structure, it gives a rather good estimate of the threshold velocity between weak and strong inertia regimes.

At last, the measured values for Darcy and Forchheimer constants are in good agreement with literature data, which reports a behavior dependent on mixing rate: Ti6Al4V-1500 shows typical values of metallic foams, whilst Ti6Al4V-700 exhibits a behavior typical for granular or fibrous media [34].

7.4. Numerical results

7.4.1. Mesh size

For the Ti6Al4V-700 sample, pores are big enough to downscale the image to a resolution of 14 μm/voxels without losing fine details. In this case the numerical simulations are performed on a sub-volume of size 384 × 384 × 384 voxels (5.38 × 5.38 × 5.38 mm^3).

As we've seen previously, about 50% of the porosity of the Ti6Al4V-1500 sample consists of small pores of size smaller than 42 μm, i.e. 6 voxels at the original resolution of 7 μm/voxel. It is therefore not possible to downscale this image if we wish to keep the finer details of the Ti6Al4V-1500. The high-resolution image cannot be used as well, since its volume is far too small to be representative. The whole image's size is 1000 × 1000 × 1000 voxels at the original resolution. Without access to a high-performance computer cluster, it is not possible to perform numerical simulations on such large image, as it contains approximately 720 × 10^6 finite volume cells. Numerical simulations are therefore carried out in smaller computational volumes of 400 × 400 × 400 voxels (2.8 × 2.8 × 2.8 mm^3), which are sufficiently large to contains a few large pores (4–5 per side). The number of cells in these sub-volumes is then approximately 46 × 10^6. Note that simulations were performed

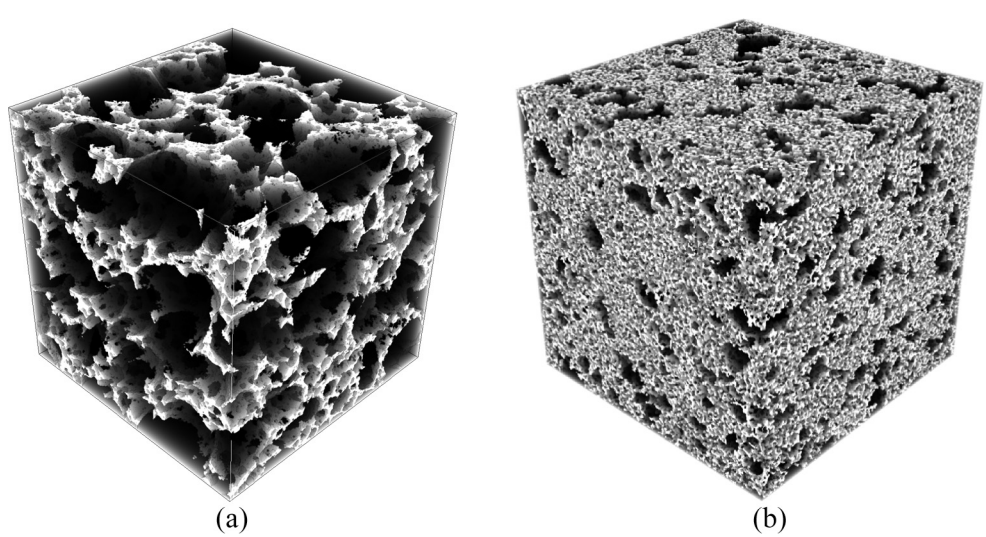

Fig. 6. (a) 3D binary representation of the Ti6Al4V-700 sample, (5.4 × 5.4 × 5.4 mm^3, resolution 14 μm/voxels – after binning of the initial reconstruction) and (b) of the low-resolution image of the Ti6Al4V-1500 sample (2.8 × 2.8 × 2.8 mm^3, resolution 7 μm/voxels – no binning. Solid matrix in white, porosity in black.

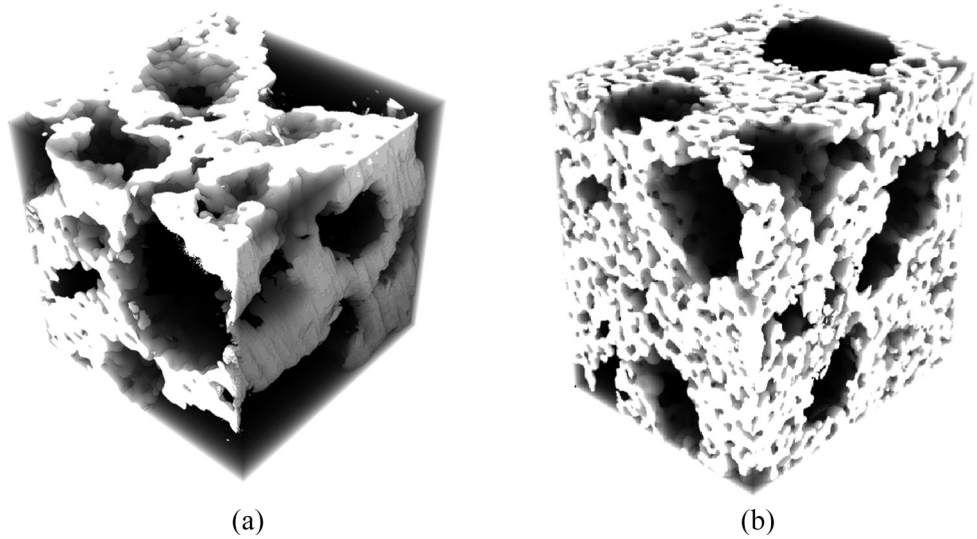

Fig. 7. (a) 3D binary representation of the high-resolution image of the Ti6Al4V-700 sample, 1.4 μm/voxel (after binning) and (b) of the Ti6Al4V-1500 sample, 7 μm/voxel (after binning). Solid matrix in white, porosity in black.

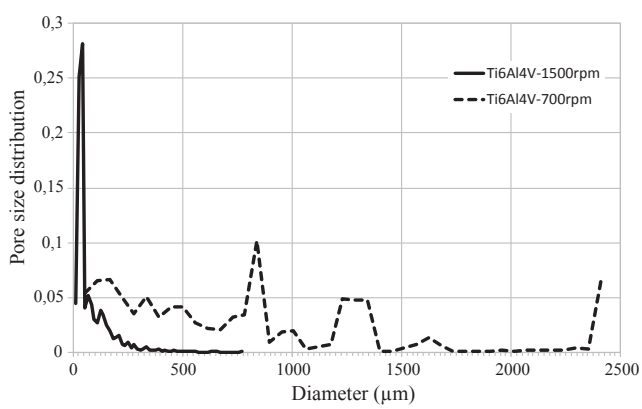

Fig. 8. Pore size distribution in low-resolution image of Ti6Al4V-1500 and Ti6Al4V-700 samples.

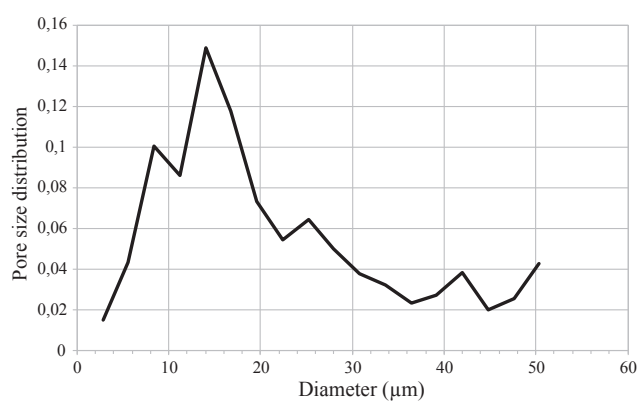

Fig. 9. Pore size distribution in high resolution image of Ti6Al4V-1500 sample, limited to pore size between 2.8 and 50 μm.

on small volumes at higher resolution (3.5 μm/voxel and 2.33 μm/voxel) to verify that the results are independent of the mesh size. Relative differences from 5% to −15% for the Darcy permeability were observed for various subvolumes of the Ti6Al4V-1500 sample for a resolution of 2.33 μm/voxel (i.e. a × 3 upscaling).

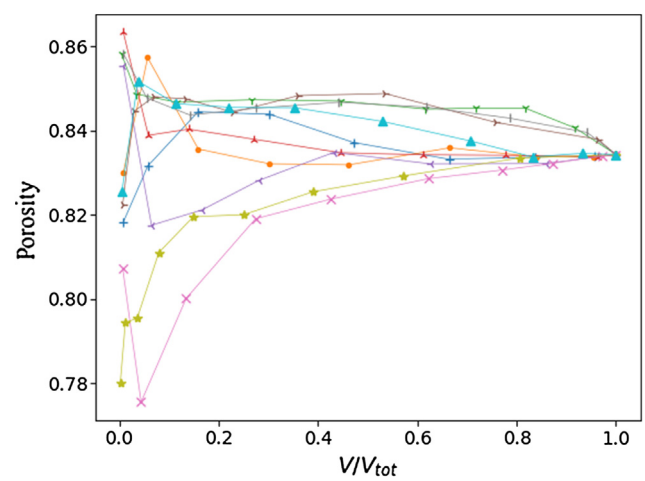

Fig. 10. Evolution of porosity in ten cubes centered randomly in the whole low-resolution image of the Ti6Al4V-700 sample versus the ratio of the cube volume over the image volume.

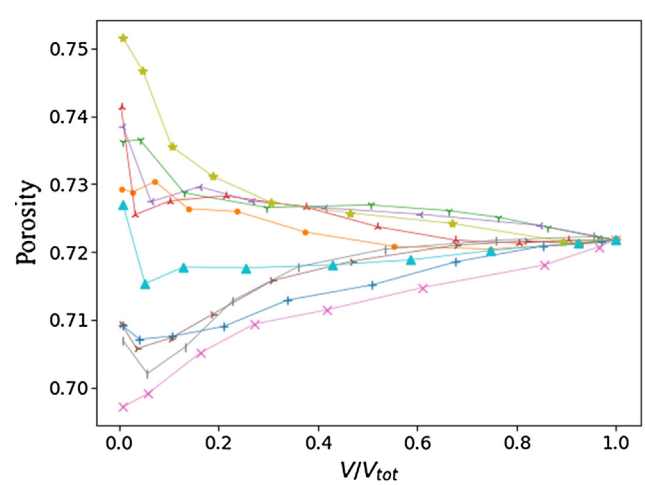

Fig. 11. Evolution of porosity in ten cubes centered randomly in the whole low-resolution image of the Ti6Al4V-1500 sample versus the ratio of the cube volume over the image volume.

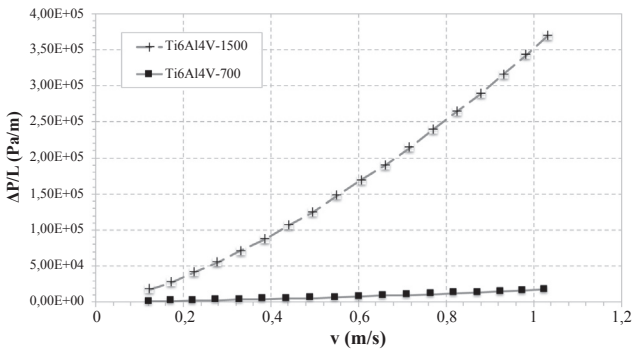

Fig. 12. Sample curves for pressure gradient versus fluid velocity for Ti6Al4V-700 and Ti6Al4V-1500 and their quadratic fittings.

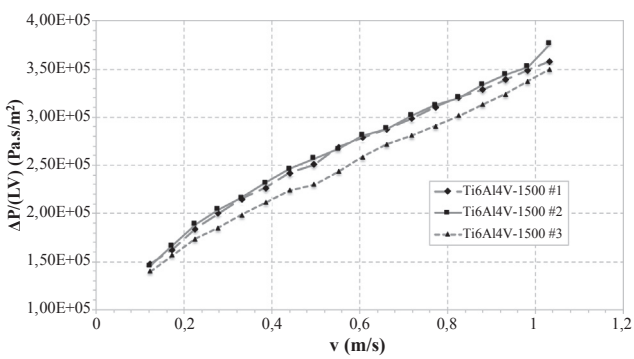

Fig. 13. Evolution of the reduced pressure gradient with superficial velocity for 3 experimental results on the Ti6Al4V-1500 sample.

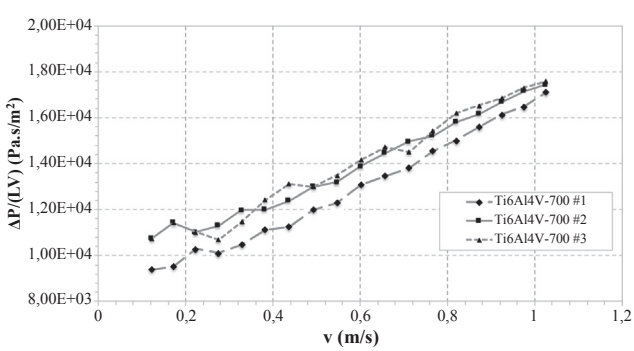

Fig. 14. Evolution of the reduced pressure drop with superficial velocity for 3 experimental results on the Ti6Al4V-1500 sample.

Table 2
Flow parameters extrapolated from experimental results (standard deviation in parenthesis).

Sample	K_D [10^{-10} m^2]	K_F [10^{-10} m^2]	β [10^4 m^{-1}]	ε
Ti6Al4V-700	21.6 (1.3)	27.2 (2.9)	0.53 (0.032)	25.8%
Ti6Al4V-1500	1.55 (0.03)	1.54 (0.14)	12.1 (0.36)	0.38%

8. Results

Results of simulations performed on the Ti6Al4V-700 as well as one of the corresponding experimental data are presented in Fig. 15. A very good agreement between the two approaches is achieved here. It is a good indication that the computational volume is sufficiently representative and that the resolution is well chosen. It is interesting to notice that the length of the computational volume is here only 2.25 times larger than the max pore size (2.4 mm) and approximately 6.7 times larger than the average pore size (792.5 μm). While we cannot be sure that the computational volume is a REV, these results indicate that a size of only a few maximum pore diameters is sufficient to achieve a good representativity. Values of Forchheimer permeability and coefficient estimated by curve fitting are $K_F = 30.5 \times 10^{-10}$ m^2 and $\beta = 6.7 \times 10^3$ m respectively, while the value of the Darcy permeability computed using Stokes flow simulation is $K_D = 27.7 \times 10^{-10}$ m^2. As in the experimental case, K_F and β are estimated in the inertia regime only while K_D is determined using Stokes flow simulation. The difference observed between experimental (21.6×10^{-10} m^2) and numerical K_D is due to the fact that K_D was estimated using only the first experimental point, which is not in pure Darcy regime. In this case, the numerical approach is better suited for the determination of the Darcy permeability.

Fig. 16 shows the evolution of pressure gradient versus measured superficial velocity for five different sub-volumes of the Ti6Al4V-1500 image, as well as the experimental results. An overview of the numerical results is presented in Table 4. Note that the absolute error on the average value of a property Z (here the permeability or Forchheimer coefficient) computed in n volumes of size V can be estimated by [35]:

Table 3
Crossover Reynolds (from weak to strong inertia regime) calculated from experimental and image porosity, as well as corresponding velocity ranges from Eq. (8) and velocity estimated using experimental curves.

Sample	Re_{Kc} (exp.)	Re_{Kc} (image)	Corresponding Threshold velocity range, m s^{-1}	Estimated velocity, m s^{-1}
Ti6Al4V-700	0.81	0.87	0.22–0.24	0.24
Ti6Al4V-1500	0.56	0.58	0.61–0.63	0.5–0.6

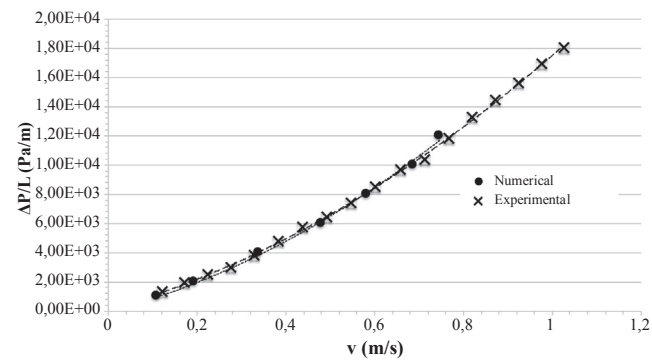

Fig. 15. Pressure gradient versus superficial velocity for the Ti6Al4V-700 sample.

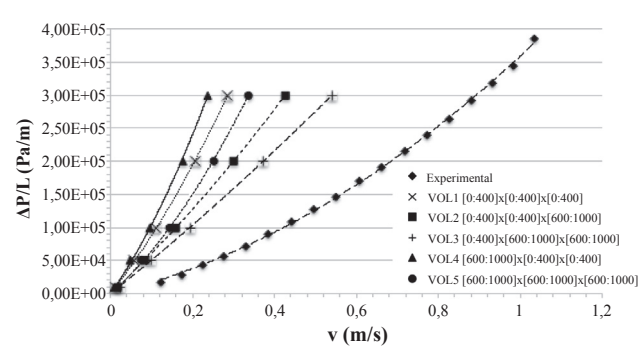

Fig. 16. Pressure gradient versus superficial velocity for the Ti6Al4V-1500 sample.

Table 4
Overview of the numerical results for the Ti6Al4V-1500 sample.

Sub-volume	Porosity	K_D from Stokes simulations $\times 10^{-11}$ (m^2)	K_F from curve fitting $\times 10^{-11}$ (m^2)	β from curve fitting $\times 10^4$ (m^{-1})
VOL1	71.8%	2.70	2.85	55.1
VOL2	74.5%	4.05	3.77	17.4
VOL3	74.2%	5.18	4.49	6.52
VOL4	69.6%	2.30	2.54	95.3
VOL5	73.7%	3.67	4.12	61.3
Average	72.8%	3.58 ± 0.39	3.56 ± 0.31	47.1 ± 28.1
Standard Deviation	1.65%	0.86	0.68	12.6

$$E_{abs} = \frac{D_Z(V)}{\sqrt{n}}$$

where $D_Z(V)$ is the standard deviation of the property Z measured in n volumes of size V.

It is clear that the curves obtained from numerical simulations show a noticeable deviation from the experimental ones. As a result, there is a significant discrepancy between the values of K_D, K_F and β estimated from numerical and experimental data. The relative difference is indeed greater than 70% for all parameters. Several factors can explain these differences: firstly, the resolution of the tomographic image of the Ti6Al4V-1500 sample is probably too low to discretize correctly the microstructure and particularly the smaller pores. With such a spatial resolution, it is likely that pores smaller than 7 µm are not detected and that the discretization effect reduces the size of pores between 7 and 14 µm, thus decreasing the apparent permeability. Note that pores which diameter is smaller than 14 µm represent 40% of the pores in the cell-wall (i.e. smaller than 50 µm), as shown in Fig. 9, which gives about 20% of the total porosity.

Secondly, the size of the computational volumes seems be smaller than the flow-dependent REV size, as it was observed in [8,36]. While the values for Darcy permeability are all of the same order of magnitude, there is a noticeable variation for the Forchheimer coefficient. Note however that these values are strongly correlated to the porosity of each sub-volume. In previous studies [8,32], it was found that the REV must contains at least 3 *average* pore diameter, whereas in our case the side of each computational volume is 3.5 times larger than the max pore diameter (approximately 800 µm). The fact that this constraint is not sufficient to achieve a good representativity in the case of the Ti6Al4V-1500 sample can be due to the double pore size distribution observed previously. However, even if the computational volumes are smaller than the REV, K_D and K_F values are quite close for all volumes and it is likely that permeability values won't change that much with an increase of the computational volume.

At last, it is worth mentioning that it is not possible to reproduce exactly the experimental boundary conditions in numerical simulations. Indeed, what is measured in the experiments is an external pressure drop across the sample, while this the internal pressure drop which is fixed in the in numerical simulations. These two quantities may differ but it is difficult to estimate if this difference is meaningful or not.

All the experimental and numerical results as well as the absolute value of the relative difference (always divided by the maximum value) are summarized in Table 5.

Figs. 17 and 18 show respectively the pressure and the velocity fields computed in the Ti6Al4V-1500 sample on a 2D cut-plane. These two fields show a behavior in agreement to other similar studies [8]. The velocity field shows important variations with areas of high velocity in the narrow pores apertures and low-velocity areas in the wake of solid ligaments. In Fig. 19, we can observe the tortuous path of streamlines in the complex microstructure.

Table 5
Summary of numerical and experimental results as well as their relative difference.

Sample	Parameters	Numerical	Experimental	Relative difference
Ti6Al4V-700	$K_D \times 10^{-10}$ (m^2)	27.7	21.6*	22%
	$K_F \times 10^{-10}$ (m^2)	30.5	27.2	11%
	$\beta \times 10^4$ (m^{-1})	0.67	0.53	21%
Ti6Al4V-1500	$K_D \times 10^{-10}$ (m^2)	0.36	1.55*	77%
	$K_F \times 10^{-10}$ (m^2)	0.36	1.54	77%
	$\beta \times 10^4$ (m^{-1})	47.1	12.1	74%

* Experimental K_D was not estimated in pure Darcy regime and is therefore under estimated.

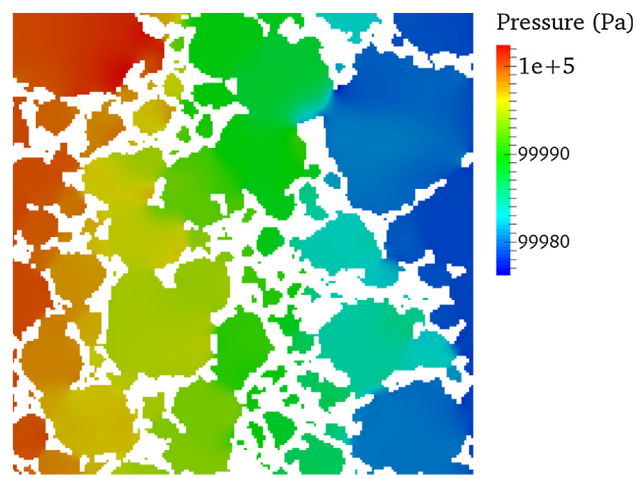

Fig. 17. Pressure field in a slice of the Ti6Al4V-700 image ($6.1 \times 6.1 mm^2$). Flow direction from left to right.

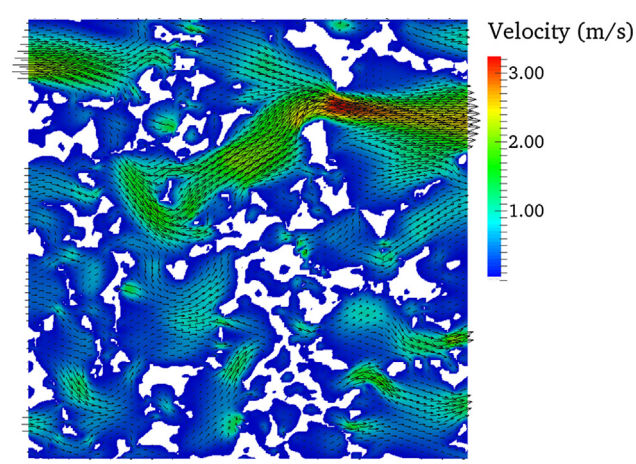

Fig. 18. Velocity field in a slice of the Ti6Al4V-700 image ($6.1 \times 6.1 mm^2$). The pore space is colored by the norm of the velocity field.

9. Conclusions

Ti6Al4V interconnected foams were produced using the gelcasting route where porosity and pore size were controlled by means of the mixer rotation speed during foaming of ovalbumine. The two used rotation speeds used gave rise to two sets of samples, Ti6Al4V-700 and Ti6Al4V-1500, with measured porosities of ~81% and 79% respectively. Low resolution and high resolution micro-tomography analyses confirmed the presence of similar level of porosities where a double pores size distribution was observed. The average pore size being larger

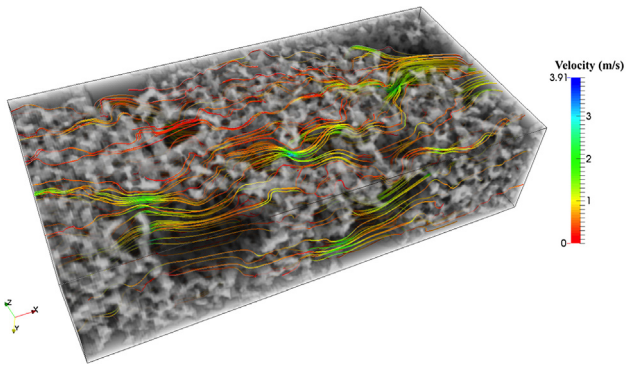

Fig. 19. 3D visualization of streamlines in the Ti6Al4V-1500. Solid phase in white.

for Ti6Al4V-700 than for Ti6Al4V-1500. For this last set of samples, high resolution images were necessary to obtain useful information concerning smaller pores size distribution. Flow regime were first identified using plots of the reduced pressure gradient vs superficial velocity. In the case of Ti6Al4V-1500 sample the inertial effect became dominant on the overall pressure drop for fluid velocities higher than 0.6 m/s. This can be attributed to the presence of pores of small size ($\leqslant 50\,\mu$m). In the case of the Ti6Al4V-700 foam, the inertial regime begins for velocities higher than 0.24 m/s approximately. These transition velocity values are very close to those calculated using correlations given in [11] for estimated porosities. Then, Darcy permeability and Forchheimer coefficient values were derived from interpolation of gas permeability data by Darcy and Forchheimer equations. Simulations performed using the Navier-Stokes equation on large volumes (46×10^6 finite volume elements) in the low-resolution tomography show very good agreement with the experimental results for the Ti6Al4V-700 foams whilst a clear deviation was observed for the Ti6Al4V-1500 samples. This last result can be attributed to the double pore size distribution of the sample which make the choice of the image's resolution quite difficult. It is indeed not possible at the moment to have both a sufficient spatial resolution to discretize the fine scale details and a sufficient volume size for representativity. However, the difference between experimental and numerical results in the case of the Ti6Al4V-1500 foam is still less than one order of magnitude, which is not so bad, in view of the discretization and representativity issue. A possible solution could be to use a multiscale approach (using upscaling techniques like volume averaging [37] or periodic homogenization [38]) to deal with the double porosity. The numerical approach coupled with micro-tomographic imaging is however an invaluable tool to study the relation between morphology and transport properties of metallic foams. As such, it could be used for process optimization of these materials.

Author contributions

The manuscript was written through contributions of all authors. All authors have given approval to the final version of the manuscript.

Funding sources

This work was funded by Università di Padova project # BIAS_SID_16_01.

Data availability

The raw/processed data required to reproduce these findings can be shared on demand.

Declarations of interest

None.

Acknowledgment

Authors wish to thank Dr. S. Corradetti and Dr. S. Carturan, Laboratori Nazionali di Legnaro, INFN-Italy for kind support in gas permeability measurements and heat treatments of foams.

References

[1] X. Pang, H. Du, Dynamic characteristics of aluminium foams under impact crushing, Compos. Part B Eng. 112 (2017) 265–277, http://dx.doi.org/10.1016/j.compositesb.2016.12.044.
[2] A. Salimon, Y. Bréchet, M.F. Ashby, A.L. Greer, Potential applications for steel and titanium metal foams, J. Mater. Sci. 40 (2005) 5793–5799, http://dx.doi.org/10.1007/s10853-005-4993-x.
[3] C. Shu, E. Wang, L. Jiang, Q. Tang, G. Sun, Studies on palladium coated titanium foams cathode for Mg–H2O2 fuel cells, J. Power Sources 208 (2012) 159–164, http://dx.doi.org/10.1016/j.jpowsour.2012.01.140.
[4] L. Biasetto, E.G. de Moraes, P. Colombo, F. Bonollo, Ovalbumin as foaming agent for Ti6Al4V foams produced by gelcasting, J. Alloys Compd. 687 (2016) 839–844, http://dx.doi.org/10.1016/j.jallcom.2016.06.218.
[5] N. Dukhan, C.A. Minjeur, A two-permeability approach for assessing flow properties in metal foam, J. Porous Mater. 18 (2011) 417–424, http://dx.doi.org/10.1007/s10934-010-9393-1.
[6] S. Rajamani, Extended Navier-Stokes Equations: Derivations and applications to Fluid Flow Problems, University of Erlangen, n.d. http://www.opus.ub.uni-erlangen.de/opus/volltexte/2013/4285/pdf/RajamaniSambasivamDissertation.pdf (accessed April 8, 2013).
[7] S. De Schampheleire, K. De Kerpel, B. Ameel, P. De Jaeger, Ö. Băgci, M. De Paepe, A discussion on the interpretation of the Darcy equation in case of open-cell metal foam based on numerical simulations, Materials 9 (2016) 15.
[8] T.P. de Carvalho, H.P. Morvan, D.M. Hargreaves, H. Oun, A. Kennedy, Pore-scale numerical investigation of pressure drop behaviour across open-cell metal foams, Transp. Porous Media 117 (2017) 311–336, http://dx.doi.org/10.1007/s11242-017-0835-y.
[9] P. Kumar, F. Topin, Investigation of fluid flow properties in open cell foams: Darcy and weak inertia regimes, Chem. Eng. Sci. 116 (2014) 793–805, http://dx.doi.org/10.1016/j.ces.2014.06.009.
[10] Y. Jobic, P. Kumar, F. Topin, R. Occelli, Predicting permeability tensors of foams using vector kinetic method, J. Phys. Conf. Ser. 745 (2016) 032140.
[11] D. Lasseux, A.A. Abbasian Arani, A. Ahmadi, On the stationary macroscopic inertial effects for one phase flow in ordered and disordered porous media, Phys. Fluids 23 (2011) 073103, http://dx.doi.org/10.1063/1.3615514.
[12] D. Lasseux, F.J. Valdés-Parada, On the developments of Darcy's law to include inertial and slip effects, Comptes Rendus Mécanique 345 (2017) 660–669, http://dx.doi.org/10.1016/j.crme.2017.06.005.
[13] P. Kumar, F. Topin, State-of-the-art of pressure drop in open-cell porous foams: review of experiments and correlations, J. Fluids Eng. 139 (2017) 111401, http://dx.doi.org/10.1115/1.4037034.
[14] A. Diani, K.K. Bodla, L. Rossetto, S.V. Garimella, Numerical investigation of pressure drop and heat transfer through reconstructed metal foams and comparison against experiments, Int. J. Heat Mass Transf. 88 (2015) 508–515, http://dx.doi.org/10.1016/j.ijheatmasstransfer.2015.04.038.
[15] S. De Schampheleire, P. De Jaeger, K. De Kerpel, B. Ameel, H. Huisseune, M. De Paepe, How to study thermal applications of open-cell metal foam: experiments and computational fluid dynamics, Materials 9 (2016), http://dx.doi.org/10.3390/ma9020094.
[16] J.-Y. Buffiere, E. Maire, J. Adrien, J.-P. Masse, E. Boller, In situ experiments with X ray tomography: an attractive tool for experimental mechanics, Exp. Mech. 50 (2010) 289–305, http://dx.doi.org/10.1007/s11340-010-9333-7.
[17] A. Etiemble, J. Adrien, E. Maire, H. Idrissi, D. Reyter, L. Roué, 3D morphological analysis of copper foams as current collectors for Li-ion batteries by means of X-ray tomography, Mater. Sci. Eng. B 187 (2014) 1–8, http://dx.doi.org/10.1016/j.mseb.2014.04.006.
[18] P. Perona, J. Malik, Scale-space and edge detection using anisotropic diffusion, IEEE Trans. Pattern Anal. Mach. Intell. 12 (1990) 629–639, http://dx.doi.org/10.1109/34.56205.
[19] J. Serra, Image Analysis and Mathematical Morphology, Academic Press, London, 1982.
[20] E. Maire, P. Colombo, J. Adrien, L. Babout, L. Biasetto, Characterization of the morphology of cellular ceramics by 3D image processing of X-ray tomography, J. Eur. Ceram. Soc. 27 (2007) 1973–1981, http://dx.doi.org/10.1016/j.jeurceramsoc.2006.05.097.
[21] Ö. Bağcı, N. Dukhan, M. Özdemir, Flow regimes in packed beds of spheres from pre-Darcy to turbulent, Transp. Porous Media 104 (2014) 501–520, http://dx.doi.org/10.1007/s11242-014-0345-0.
[22] M.D.M. Innocentini, A.R.F. Pardo, V.C. Pandolfelli, Influence of air compressibility on the permeability evaluation of refractory castables, J. Am. Ceram. Soc. 83 (2000) 1536–1538, http://dx.doi.org/10.1111/j.1151-2916.2000.tb01426.x.

[23] J.-P. Bonnet, F. Topin, L. Tadrist, Flow laws in metal foams: compressibility and pore size effects, Transp. Porous Media 73 (2008) 233–254, http://dx.doi.org/10.1007/s11242-007-9169-5.
[24] M.D.M. Innocentini, L.P. Lefebvre, R.V. Meloni, E. Baril, Influence of sample thickness and measurement set-up on the experimental evaluation of permeability of metallic foams, J. Porous Mater. 17 (2010) 491–499, http://dx.doi.org/10.1007/s10934-009-9312-5.
[25] L. Biasetto, M.D.M. Innocentini, W.S. Chacon, S. Corradetti, S. Carturan, P. Colombo, A. Andrighetto, Gas permeability of lanthanum oxycarbide targets for the SPES project, J. Nucl. Mater. 440 (2013) 70–80, http://dx.doi.org/10.1016/j.jnucmat.2013.04.038.
[26] J. Li, Q. Zhang, Z.-Q. Zhai, An efficient SIMPLER-revised algorithm for incompressible flow with unstructured grids, Numer. Heat Transf. Part B Fundam. 71 (2017) 425–442, http://dx.doi.org/10.1080/10407790.2017.1293965.
[27] H.K. Versteeg, W. Malalasekera, An Introduction to Computational Fluid Dynamics: The Finite Volume Method, second ed., Pearson Education, 2007. http://ftp.demec.ufpr.br/disciplinas/TM701/Versteeg%20H%20K%20,%20Malalasekera%20W%20Introduction%20To%20Computational%20Fluid%20Dynamics%20The%20Finite%20Volume%20Method%20(Longman,%201995)(T)(267S).pdf (accessed June 21, 2016).
[28] P. Sepulveda, J.G. Binner, Processing of cellular ceramics by foaming and in situ polymerisation of organic monomers, J. Eur. Ceram. Soc. 19 (1999) 2059–2066, http://dx.doi.org/10.1016/S0955-2219(99)00024-2.
[29] C. Mabille, F. Leal-Calderon, J. Bibette, V. Schmitt, Monodisperse fragmentation in emulsions: mechanisms and kinetics, EPL Europhys. Lett. 61 (2003) 708.
[30] U.T. Gonzenbach, A.R. Studart, E. Tervoort, L.J. Gauckler, Tailoring the microstructure of particle-stabilized wet foams, Langmuir 23 (2007) 1025–1032, http://dx.doi.org/10.1021/la0624844.
[31] S. Meille, M. Lombardi, J. Chevalier, L. Montanaro, Mechanical properties of porous ceramics in compression: on the transition between elastic, brittle, and cellular behavior, J. Eur. Ceram. Soc. 32 (2012) 3959–3967, http://dx.doi.org/10.1016/j.jeurceramsoc.2012.05.006.
[32] E. Brun, J. Vicente, F. Topin, R. Occelli, M.J. Clifton, Microstructure and transport properties of cellular materials: representative volume element, Adv. Eng. Mater. 11 (2009) 805–810, http://dx.doi.org/10.1002/adem.200900131.
[33] P. Kumar, F. Topin, Micro-structural impact of different strut shapes and porosity on hydraulic properties of Kelvin-like metal foams, Transp. Porous Media 105 (2014) 57–81, http://dx.doi.org/10.1007/s11242-014-0358-8.
[34] M. Scheffler, P. Colombo (Eds.), Cellular Ceramics: Structure, Manufacturing, Properties and Applications, Wiley-VCH, Weinheim, 2005.
[35] T. Kanit, S. Forest, I. Galliet, V. Mounoury, D. Jeulin, Determination of the size of the representative volume element for random composites: statistical and numerical approach, Int. J. Solids Struct. 40 (2003) 3647–3679, http://dx.doi.org/10.1016/S0020-7683(03)00143-4.
[36] G. Laschet, J. Sauerhering, O. Reutter, T. Fend, J. Scheele, Effective permeability and thermal conductivity of open-cell metallic foams via homogenization on a microstructure model, Comput. Mater. Sci. 45 (2009) 597–603, http://dx.doi.org/10.1016/j.commatsci.2008.06.023.
[37] S. Whitaker, The Forchheimer equation: a theoretical development, Transp. Porous Media 25 (1996) 27–61.
[38] E. Sanchez-Palancia, Non-homogeneous media and vibration theory, 1980.